High-sensitivity photonic crystal fiber sensor based on surface plasmon resonance[*]

FENG Huanting, GAO Jiachen, and MING Xianbing[**]

School of Physical Science and Technology, Tiangong University, Tianjin 300387, China

In this paper, we propose a photonic crystal fiber (PCF) sensor based on the surface plasmonic resonance (SPR) effect for simultaneous temperature and refractive index (RI) measurement. The coupling characteristics and sensing performance of the sensor are analyzed using the full vector finite element method (FEM). The sensor provides two channels for independent measurement of RI and temperature. When operating independently, channel I supports *y*-polarized light with a sensitivity of up to 7 000 nm/RIU for detecting RI, while channel II supports *x*-polarized light with a sensitivity of up to 16 nm/°C for detecting temperature. Additionally, we investigate the influence of gold layer thickness on the sensing performance to optimize the sensor.

With the increasing demand for high quality in both production and daily life, as well as the rapid development of high-tech fields, there is an urgent need for highly sensitive sensors in today's era. Photonic crystal fiber (PCF) combines the advantages of photonic crystals and optical fibers, such as excellent optical properties, miniaturization, small size, and easy integration. PCF has gradually gained extensive attention from researchers by overcoming limitations brought about by conventional optical fibers, such as low-loss guidance of light. In recent years, the research focus has shifted towards concepts, such as microstructure, multi-material integration, and multi-functionality. Surface plasma technology-based PCF sensing has emerged as a prominent area of scientific investigation and is regarded as an advanced direct sensing technique[1,2].

Surface plasmon waves (SPWs) are transmission wave modes that propagate continuously along the surface of metallic materials and dielectrics, exhibiting sensitivity to small changes in the refractive index (RI) of the surrounding medium[3]. In simple terms, incident light is irradiated onto the metal material's surface under phase-matching conditions, allowing it to propagate energy according to the structure of the metal material. This phenomenon is known as surface plasmonic resonance (SPR). By combining the sensitivity of SPWs with the optical properties of optical fibers, Jorgenson pioneered the first SPR-based optical fiber chemical sensor in 1993. The design utilized a smaller sensing element, streamlining optical design and reducing sensing volume for remote and in situ detection[4]. Conventional sensors utilize a prismatic structure based on the attenuated total reflection (ATR) principle, which for commercial SPR sensors necessitates numerous optics and mechanical components, resulting in large size and high cost. The introduction of PCF disrupts the traditional optical fiber landscape and expands the potential applications in sensing. PCF is a novel type of optical fiber with flexible design capabilities, allowing for customizable pore structures around the core to control energy coupling between the fiber core and plasma for practical use. With this flexibility in fiber structure design, dispersion can be controlled to achieve high degrees of flexibility that further enhance performance in fiber optic sensing[5]. So far, many single data measurements have been proposed in research papers, such as RI[6,7], temperature[8], magnetic field[9], colony-forming[10], gas[11], biosensing[12], etc. In practice, the operating temperature affects almost all uncompensated sensors, which is also known as temperature cross-sensitivity. To solve this headache, methods such as temperature compensation or multi-parameter measurement of the sensor are generally used. YANG et al[13] proposed a D-shaped microstructured optical fiber surface plasma sensor for simultaneous measurement of RI and temperature. When the thickness of the gold layer exceeds 40 nm, the RI sensitivity reaches 2 400 nm/RIU, while the temperature sensitivity is 2 nm/°C. SPR sensors are flexible in their structural design and allow sensitivity to be adjusted by modifying their external shape[14,15].

PCF has been revolutionizing traditional fiber optic applications by fostering innovative thinking modes. Its exceptional optical properties enable remarkable advancements in biomedical research, communication systems, imaging technologies, detection methods, metrology practices, and other fields. Furthermore, it is worth noting that PCF development remains ongoing with unpredictable potential. In this paper, we propose an optimized structure for a D-shaped PCF-SPR sensor to achieve simultaneous measurement of temperature and RI. Our approach expands the temperature detection range and improves sensitivity data accuracy while simplifying the structure design. Moreover, considering industrial production feasibility, our designed PCF optic sensors hold promising practicality.

Fig.1 shows the schematic structure of the D-shaped PCF which can detect both RI and temperature changes. Channel I, located in the D-shaped region, facilitates RI change detection, while channel II utilizes air holes located in the center of the optical fiber coated with temperature-sensitive liquid chloroform to detect temperature changes. Chloroform possesses a large thermal radiation coefficient (dn/dT) of -6.328×10^{-4}/K. In addition, it can be noted that the air holes located in the fiber core are closer to the D-shaped region, which can enhance the interaction between the swift field and the metal film in such a way that the transport coupling between the two is strengthened and the SPR effect is enhanced. The sensor cladding has three layers of pores, the optical fiber diameter r=9 μm, the perfectly matched layer (PML) r_p=1 μm, the spacing Λ=2 μm for each layer, the diameter d is set to 0.4Λ, and the thicknesses of gold m_1 and m_2 used for plasma excitation material are both 40 nm. The chemical stability of gold is better than silver, it does not easily oxidize when exposed to air over extended periods. Additionally, gold exhibits larger resonant wavelength shifts which contribute to improved sensitivity[12-14,16-18]. The sensor can be prepared by stacked drawing and polishing techniques for D-shaped optical fiber, while a gold film is clad on the outside of the D-shaped optical fiber as a plasma excitation material; the desired thickness of the gold film is obtained by precisely controlling the deposition time and the deposition rate by using a conventional wet chemical deposition technique[19]. The sensor can be prepared using stacked pulling and polishing techniques for the optical fiber and D-shaped region; the gold film can be prepared by conventional wet chemical deposition technique by controlling the deposition time and deposition rate exactly to the required thickness of the gold film[20]. The background material used for this sensor is SiO$_2$ in its molten state and its RI is calculated by the Sellmeier equation[19].

$$n_S^2 = A + B(1 - C / \lambda^2) + D(1 - E / \lambda^2), \qquad (1)$$

$$n_T = n_0 + dn / dT \cdot (T - T_0), \qquad (2)$$

where A=1.315 52, B=0.788 404, C=1.101 99×10^{-2}, D=0.913 16, E=100[19], λ is the wavelength of the light incident in free space, and n_S is the RI of SiO$_2$. n_0 is the

RI at room temperature, and n_T is the RI at temperature T. The RI of chloroform can be calculated by Eq.(2). The RI is different for different ambient temperatures, and the RI of gold refers to the Drude-Lorentz model[19]. The research core of the whole paper is to simulate the D-shaped PCF-SPR sensor. The structural model was calculated using the full vector finite element method (FEM). The boundary conditions are PML and scattering boundary condition (SBC), both of which are used to model the external space and absorb excess light waves. When the modal analysis is performed on a plane, light travels in a direction perpendicular to the plane that is the z-axis. The effective RI profile relations for the core and SPP modes of different orders as well as the losses of the x-polarized fundamental mode and y-polarized fundamental mode are shown in Fig.2, and the losses are calculated by

$$\alpha_{loss} (dB/ cm) = 8.686 \times k_0 \cdot Im[n_{eff}], \qquad (3)$$

where k_0=2π/λ, and Im[n_{eff}] is the imaginary part of the RI.
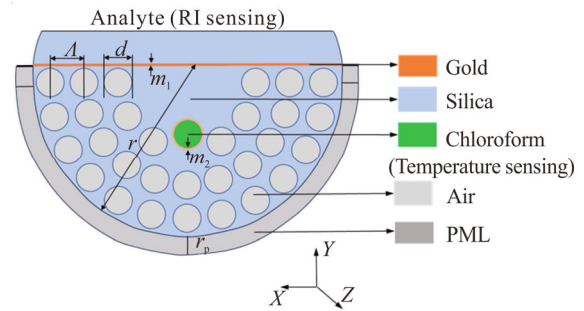
**Fig.1 Schematic cross-section of a modified D-shaped PCF sensor in *x-y* plane**

As can be seen in Fig.2(a), due to the asymmetric structure of the sensor, the effective RI of the x-polarized and y-polarized fundamental modes are different in the real part, and thus a strong birefringence phenomenon can be seen. As can be seen from the loss curve in Fig.2(b), it can be observed that the loss curve plots of both x-polarized and y-polarized fundamental modes contain raised loss peaks, which is since the energy of the fiber core is coupled to the metal surface most at the resonance wavelength, resulting in a huge drop in the energy of the fiber core, and the loss value of the fiber core will be increased dramatically, and thus sharp peaks appear in the loss spectra. At the same time, the wavelength corresponding to the loss peak is the resonance wavelength at which the SPR effect occurs between the core and the metal material under the current conditions. Also at the resonance wavelength positions, the real part of the RI jumps (see 660 nm, 740 nm, and 760 nm in Fig.2(a)). It can be seen that the loss peaks in channel I are sharper and the corresponding transmission losses are larger, which indicates that the core and SPP modes are more strongly coupled in channel I than in channel II. The x-polarized and y-polarized fundamental modes have two loss peaks in the 500—800 nm band, and at the

resonance wavelength corresponding to each of these peaks, the core mode transmits the most energy to the SPP mode of different order, and the coupling degree between the two modes is the strongest and the corresponding modes have been shown in Fig.2(b), where the real part of RI also jumps (see 660 nm, 740 nm, and 760 nm). The corresponding modes have been shown in Fig.2(a).

Fig.3 illustrates the coupling of the SPP mode to the fiber core mode. The red arrow in the figure represents the direction of the electric field. As can be seen from Fig.3, the core mode located in the fiber core is divided into two modes with completely different directions in the process of light transmission, one of which has an electric field direction parallel to the *x*-axis and is called the *x*-polarized fundamental mode (see Fig.3(f)). The other mode has an electric field direction parallel to the *y*-axis and is called the *y*-polarization fundamental mode (see Fig.3(g)). In the following sections, the *x*-polarized fundamental mode is referred to as *x*-pol for convenience; and the *y*-polarized fundamental mode is referred to as *y*-pol. Because the core mode is divided into two orthogonal modes, the sensor has strong birefringent properties.

Fig.4 shows the movement of *x*- and *y*-pols loss peaks at different ambient temperatures and RI. As can be seen from Fig.4(a), when the external ambient temperature is 20 °C and the RI is varied from 1.36 to 1.37, respectively, it can be observed that the loss peak of *y*-pols moves from 640 nm to 660 nm, $\Delta\lambda=20$ nm, whereas the loss spectrogram of *x*-pol remains unchanged. As can be seen in Fig.4(b), when the RI is 1.37 and the temperature is varied from 20 °C to 30 °C, respectively, it can be observed that the loss peak of *x*-pol moves from 862 nm to 920 nm at $\Delta\lambda=58$ nm, and one of the loss peaks of *y*-pol produces a slight shift due to the small portion of the *y*-pol energy coupled to the temperature-sensitive channel.

Tab.1 demonstrates the shifting of the resonance wavelengths of *x*-pol and *y*-pol when *T* rises from 20 °C to 30 °C and RI rises from 1.36 to 1.37. Thus it can be shown that the channel I changes only with the RI and does not change with the temperature; similarly, it can be shown that the channel II changes only with the external ambient temperature.
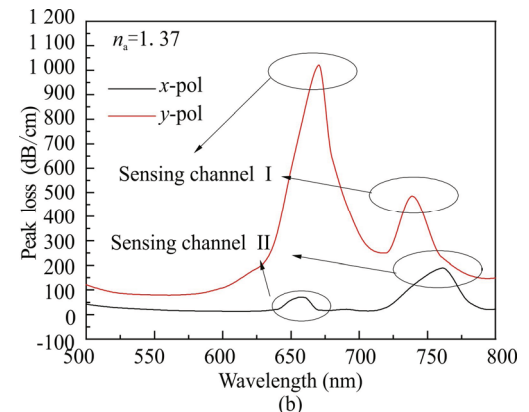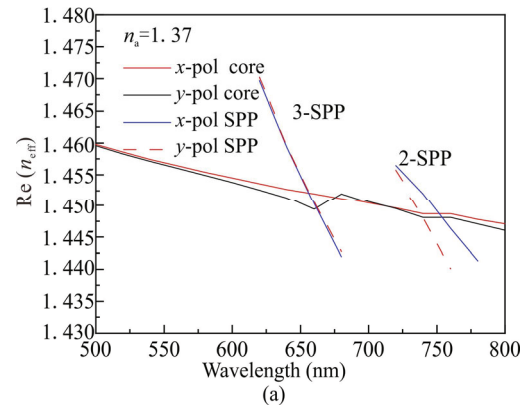
Fig.2 (a) Effective RI real part curves of core modes and SPP modes of different orders; (b) Loss spectra of *x*- and *y*-pols
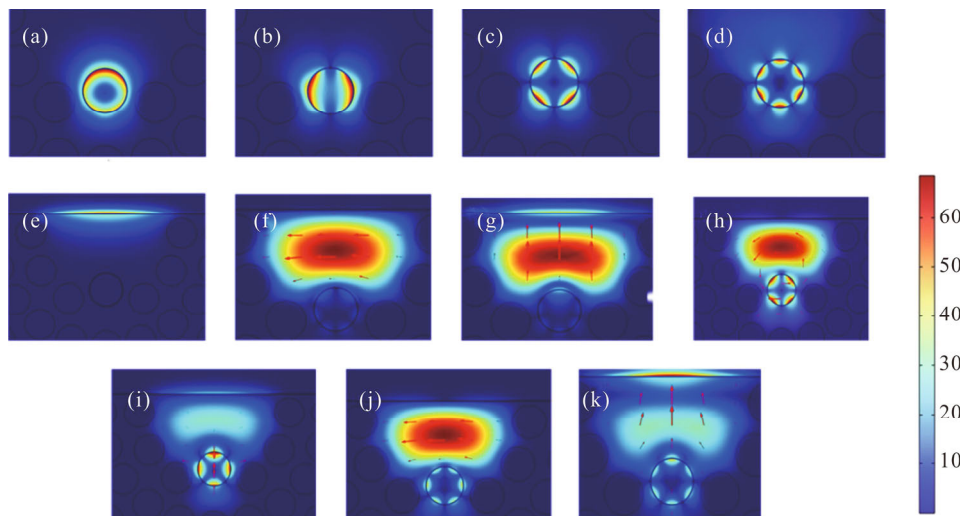

Fig.3 Electric field distributions of SPP modes at sensing region Ⅱ: (a) 0th-order SPP mode; (b) 1st-order SPP mode; (c) 2nd-order SPP mode; (d) 3rd-order SPP mode; Sensing region I: (e) SPP mode; (f) Core mode of *x*-pol; (g) Core mode of *y*-pol; Sensing region II: (h) 2nd-order core mode of *x*-pol; (i) 2nd-order core mode of *y*-pol; (j) 3rd-order core mode of *x*-pol; (k) 3rd-order core mode of *y*-pol (The red arrow represents the direction of the electric field)

The sensors were analyzed below at different temperatures and RI conditions, respectively, and the resonance wavelengths at different RI or temperatures were recorded with linear and nonlinear fits. The RI sensitivity (see Eq.(4)) and temperature sensitivity (see Eq.(5)) can be calculated from the shifts of the resonance peaks.

$$S_n = \Delta\lambda / \Delta n, \tag{4}$$

$$S_T = \Delta T / \Delta n, \tag{5}$$

where S_n is the RI sensitivity, S_T is the temperature sensitivity, $\Delta\lambda$ is the offset of the resonance wavelength, ΔT is the temperature change, and Δn is the change of RI in the external environment.
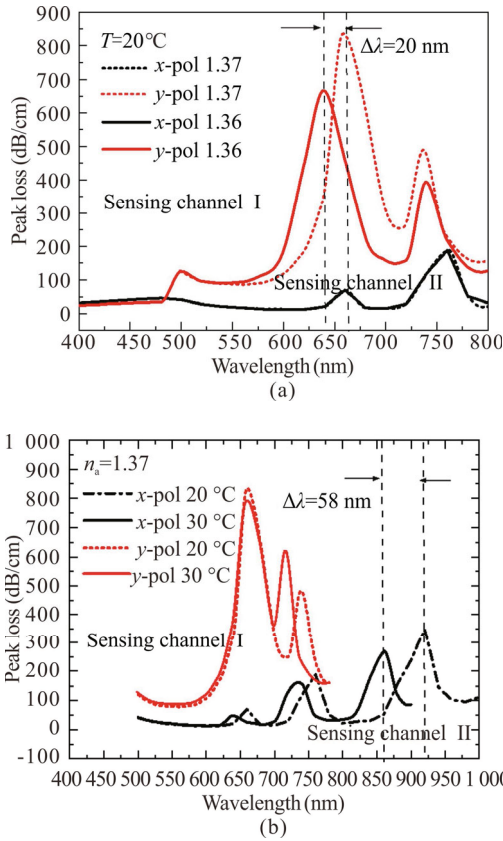

Fig.4 Loss spectra of *x*- and *y*-pol core modes (a) at *T*=20 °C when RI changes from 1.36 to 1.37, and (b) at RI=1.37 when temperature changes from 20 °C to 30 °C

Tab.1 Resonant wavelengths of *x*- and *y*-pol when the temperature changes from 20 °C to 30 °C and RI changes from 1.36 to 1.37

| Sensing channels		Channel I		Channel Ⅱ	
Temperature (*T*)	RI	*x*-pol (nm)	*y*-pol (nm)	*x*-pol (nm)	*y*-pol (nm)
20 °C	1.36	920	640	920	640
30 °C	1.37	920	660	920	660
	1.37	862	660	862	660

Fig.5 shows the fundamental core mode loss spectra when the temperature is changed from −15 °C to 10 °C.

It can be seen from the figure that the position of the resonance peak changes when the temperature changes. Fig.6 shows the sensitivity curve of the resonance wavelength of *x*-pol fitted with temperature. From the figure, it can be seen that the shift of the resonance wavelength of *x*-pol in the range of −15—10 °C, the resonance wavelength undergoes a substantial blue shift with the increasing temperature, while the resonance wavelength of *y*-pol remains unchanged at 660 nm. The average sensitivity in the range of −15—10 °C can be calculated as 8.4 nm/°C by Eq.(5). In the range of −15—10 °C, the fitting function is linear, and the expression of the sensitivity curve is *y*=−16*x*+1 020. The slope of the straight line is the corresponding sensitivity, with values up to 16 nm/°C. The sensitivity is expressed as a nonlinear function in the range from −10 °C to 10 °C. In the range from −10 °C to 10 °C, the fitting function is nonlinear and the sensitivity curve is expressed as *y*=0.085 7*x*²−6.2*x*+1 111.714. The correlation coefficient is 0.995 3, and the sensitivity curve can be obtained by derivation of the curvilinear relationship of *y*=0.172*x*−6.2. It is seen that a maximum value of 6.2 nm/°C is achieved when the temperature is 0 °C.
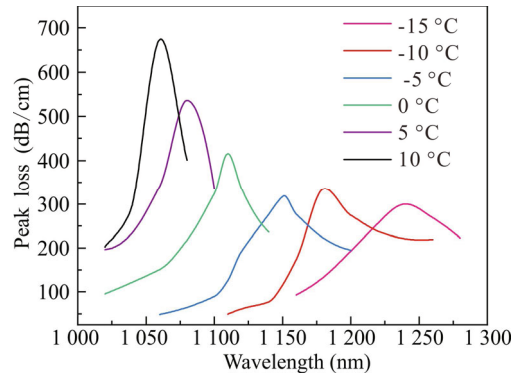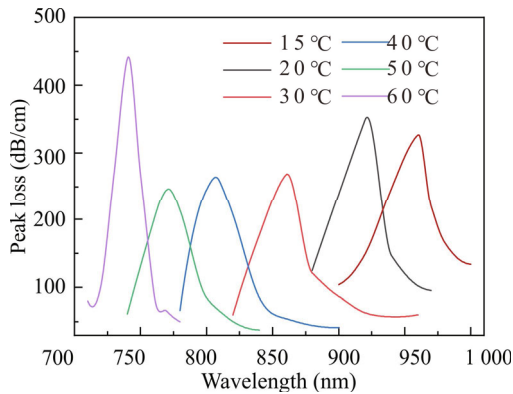

Fig.5 Fundamental core mode loss spectra at −15—10 °C
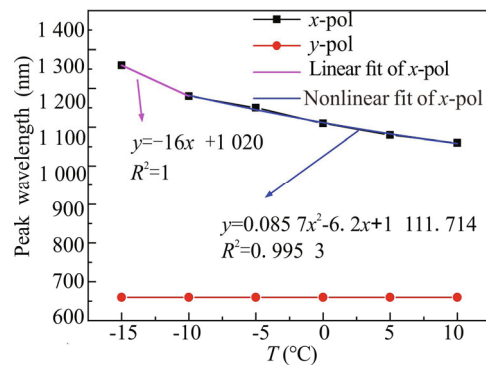
Fig.6 Shift of the resonance wavelength from −15 °C to 10 °C

Fig.7 shows the fundamental core mode loss spectra when the temperature is changed from 15 °C to 60 °C. Fig.8 shows the shift of the *x*-pol resonance wavelength from 15 °C to 60 °C. It can be seen from the figure that

the resonance wavelength appears to be blue-shifted as the temperature increases, and this result is consistent with that in Fig.6. When the temperature is higher than 60 °C, the shift of the resonance wavelength will be saturated, so the maximum detection temperature of the sensor is 60 °C. The average sensitivity in the range of 15—60 °C can be calculated from Eq.(5) to be about 4.9 nm/°C. Fitting the data of *x*-pol resonance wavelength in the range of 15—25 °C, the expression of the sensitivity relation curve is $y=-8x+1\,080$, and the temperature sensitivity reaches 8 nm/°C.

Fig.7 Fundamental core mode loss spectra at 15—60 °C
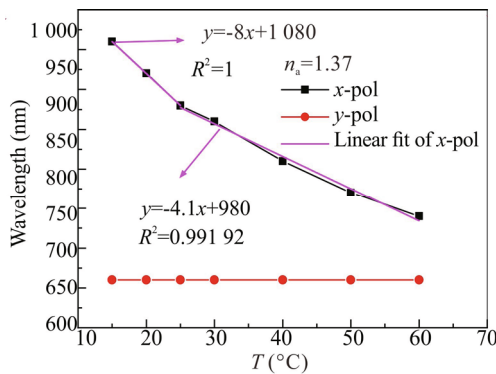

**Fig.8 Shift of the resonance wavelength from 15 °C to 60 °C**

Fig.9 shows the relationship between RI and *y*-pol resonance wavelength, which increases from 1.345 to 1.40 at a rate of 0.05. From the curves in the figure, it can be seen that the resonance wavelength of *x*-pol stays at 660 nm without shifting and the resonance wavelength of *y*-pol is red-shifted and will no longer shift as the RI becomes progressively larger, which is in agreement with the results of Ref.[21]. In the range of 1.37≤RI≤1.375, the sensitivity equation of RI versus resonance wavelength was obtained by fitting the function of $y=7\,000x-8\,930$, and the slope of the curve is 7 000. So the slope of the curve is the RI sensitivity value of 7 000 nm/RIU.

The optimization of the sensor parameters is also the focus of this study as the thickness of the metallic material has a significant effect on the sensitivity of the sen-

sor. The values in Fig.10 represent the positions where the resonance peaks are located. By using Eq.(4) and Eq.(5), it can be concluded that the sensitivity is directly proportional to the size of the wavelength shift, so the larger the resonance wavelength shift, the higher the sensitivity will be accordingly. The offset of the resonance peak at 40 nm is $\Delta\lambda=50$ nm, so the metal film of 40 nm thickness is the best choice. Meanwhile, the loss spectrum has a tendency to increase and then decrease, reaches the maximum at 40 nm, and the transmission coupling efficiency is the highest when 40 nm is selected. The trend of increasing and then decreasing in Fig.10 is caused by the limited penetration depth of the core mold.
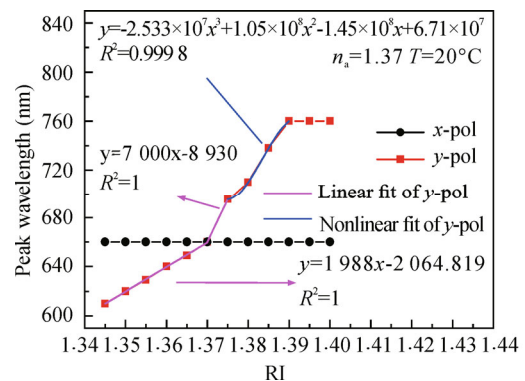
Fig.9 Resonance wavelength shift when RI changes from 1.345 to 1.40 with a step of 0.005
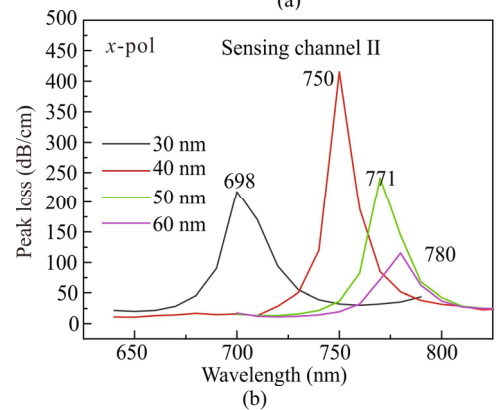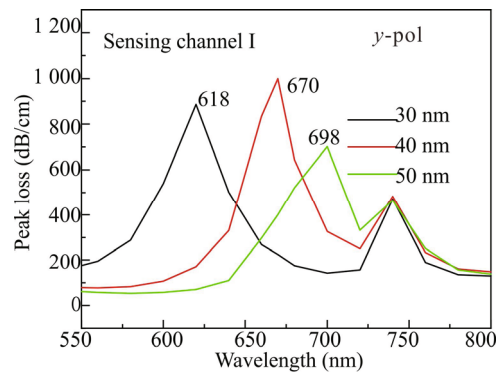

Fig.10 (a) m_2=40 nm, loss spectra corresponding to different gold film thicknesses m_1; (b) m_1=40 nm, loss spectra corresponding to different gold film thicknesses m_2

Eq.(4) shows that the greater the offset, the greater the sensitivity. We conclude that when studying the influence of gold layer thickness m_1 and m_2 on sensor sensitivity, the emphasis should be placed on the value of the offset. As shown in Fig.11, both $\Delta\lambda_1$ and $\Delta\lambda_2$ exhibit a similar trend, increasing with gold layer thickness before stabilizing. The wavelength sensitivity values also follow this trend. When the thickness of the gold layer is 40 nm, the coupling efficiency is larger and the wavelength sensitivity is larger, so a gold layer thickness of 40 nm is more favorable to the performance of the sensor. When the thickness of the gold layer is 40 nm, the temperature sensitivity can reach up to 16 nm/°C, and the RI sensitivity reaches 7 000 nm/RIU.

In this study, the D-type PCF optical sensing structure based on plasma resonance is improved. Compared with the conventional sensors, the sensor proposed in this paper has the following advantages. Channel I and channel II can work simultaneously, avoiding cross-sensitivity to a larger extent. The sensitivity can be
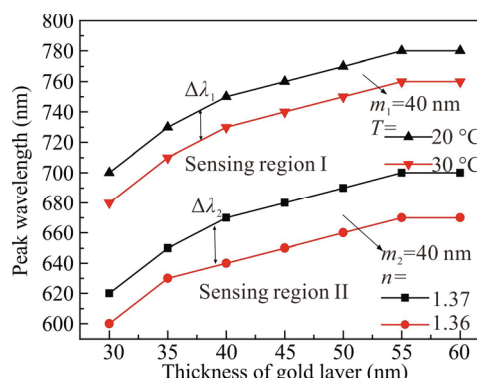
Fig.11 The *x*- and *y*-pol resonance wavelengths change curves when the gold layer thickness changes from 30 nm to 60 nm at 20 °C and 30 °C, or when RI is 1.36 and 1.37

Tab.2 Performance comparison among the proposed sensor and other present PCF-SPR sensors

Ref.	Structure style	RI range	T range (°C)	Layer of metal	Channel I (nm/RIU)	Channel II (nm/°C)
[15]	D-shaped coated double-channel	1.33—1.35	20—60	Au	2 400	2
[22]	D-shape temperature and RI SPR sensor	1.35—1.46	−50—50	Au	5 000	3.0
[23]	Open channels with plasmonic materials	1.33—1.39	-	Au	6 000	
[24]	Gold-coated D-shaped structure		0—60	Au		10.61
[25]	Gold coating structure	1.35—1.40	20—60	Au	4 520	4.83
[26]	Gold coating structure (only a single variable is detected)	1.32—1.40	-	Au	9 000	-
Proposed	D-shaped coated double-channel	1.34—1.39	−15—60	Au	7 000	16

calculated directly from the offset of the resonance peaks without the need for complex matrix equations. The sensor can detect temperature and RI at the same time, which is economical and practical. The structure has a D-shaped polished surface coated with a gold film and a gold film on the outside of only one hole, which reduces the difficulty of the coating operation and makes it operable, and the D-shaped polished surface also enhances the SPR effect to improve the sensitivity and practicality. The simulation data in this study show that the sensor has good numerical performance in temperature and external environment detection, which is expected to be useful in the field of sensing.

Ethics declarations

Conflicts of interest

The authors declare no conflict of interest.

References

[1] RUSSELL P. Photonic crystal fibers[J]. Science, 2003, 299(5605): 358-362.

[2] CERQUEIRA S A. Recent progress and novel applications of photonic crystal fibers[J]. Reports on progress in physics, 2010, 73(2): 024401.

[3] ERDMAINS M, VIEGAS D, HAUTAKORPI M, et al. Comprehensive numerical analysis of a surface-plasmon-resonance sensor based on an H-shaped optical fiber[J]. Optics express, 2011, 19(15): 13980-13988.

[4] JORGENSON R C, YEE S S. A fiber-optic chemical sensor based on surface plasmon resonance[J]. Sensors and actuators B: chemical, 1993, 12(3): 213-220.

[5] LIU Y, LI S, CHEN H, et al. Surface plasmon resonance induced high sensitivity temperature and refractive index sensor based on evanescent field-enhanced photonic crystal fiber[J]. Journal of lightwave technology, 2019, 38(4): 919-928.

[6] YAN X, LI B, CHENG T L, et al. Analysis of high sensitivity photonic crystal fiber sensor based on surface plasmon resonance of refractive indexes of liquids[J].

Sensors, 2018, 18(9): 2922.

[7]   LIU C, SU W, WANG F, et al. Birefringent PCF-based SPR sensor for a broad range of low refractive index detection[J]. IEEE photonics technology letters, 2018, 30(16): 1471-1474.

[8]   CHAUDHARY V S, KUMAR D, KUMAR S. Gold-immobilized photonic crystal fiber-based SPR biosensor for detection of malaria disease in human body[J]. IEEE sensors journal, 2021, 21(16): 17800-17807.

[9]   WANG B T, WANG Q. Sensitivity-enhanced optical fiber biosensor based on coupling effect between SPR and LSPR[J]. IEEE sensors journal, 2018, 18(20): 8303-8310.

[10]   KUMAR S, GUO Z, SINGH R, et al. MoS_2 functionalized multicore fiber probes for selective detection of shigella bacteria based on localized plasmon[J]. Journal of lightwave technology, 2021, 39(12): 4069-4081.

[11]   ZHANG C, CHEN X, LIU X, et al. High sensitivity hydrogen sensor based on tilted fiber Bragg grating coated with $PDMS/WO_3$ film[J]. International journal of hydrogen energy, 2022, 47(9): 6415-6420.

[12]   AHMED F, AHSANI V, NAZERI K, et al. Monitoring of carbon dioxide using hollow-core photonic crystal fiber Mach-Zehnder interferometer[J]. Sensors, 2019, 19(15): 3357.

[13]   YANG X, LU Y, LIU B, et al. Simultaneous measurement of refractive index and temperature based on SPR in D-shaped MOF[J]. Applied optics, 2017, 56(15): 4369-4374.

[14]   LIU X L, LIU J, YANG H M, et al. Design of a high-performance graphene/SiO_2-Ag periodic grating/MoS_2 surface plasmon resonance sensor[J]. Applied optics, 2022, 61(23): 6752-6760.

[15]   ISALM N, ARIF M F H, YOUDUF M A, et al. Highly sensitive open channel based PCF-SPR sensor for analyte refractive index sensing[J]. Results in physics, 2023, 46: 106266.

[16]   RIFAT A A, AHMES R, MAHDIRAJI G A, et al. Highly sensitive D-shaped photonic crystal fiber-based plasmonic biosensor in visible to near-IR[J]. IEEE sensors journal, 2017, 17(9): 2776-2783.

[17]   CHAUDHARY V S, KUMAR D, PANDEY B P, et al. Advances in photonic crystal fiber-based sensor for detection of physical and biochemical parameters-a review[J]. IEEE sensors journal, 2022, 23(2): 1012-1023.

[18]   QIU H W, XU S C, JIANG S Z, et al. A novel graphene-based tapered optical fiber sensor for glucose detection[J]. Applied surface science, 2015, 329: 390-395.

[19]   GHOSH G, ENDO M, IWASAKI T. Temperature-dependent Sellmeier coefficients and chromatic dispersions for some optical fiber glasses[J]. Journal of lightwave technology, 1994, 12(8): 1338-1342.

[20]   LIU B H, JIANG Y X, ZHU X S, et al. Hollow fiber surface plasmon resonance sensor for the detection of liquid with high refractive index[J]. Optics express, 2013, 21(26): 32349-32357.

[21]   VIAL A, GRIMAULT A S, MACIAS D, et al. Improved analytical fit of gold dispersion: application to the modeling of extinction spectra with a finite-difference time-domain method[J]. Physical review B, 2005, 71(8): 085416.

[22]   MIAO Y P, ZHANG H, LIN J C, et al. Simultaneous measurement of temperature and magnetic field based on a long period grating concatenated with multimode fiber[J]. Applied physics letters, 2015, 106(13): 123410.

[23]   ISLAM N, MASUM M M U, ARIF M F H, et al. Enhanced sensitivity of open channel SPR-based PCF sensor employing plasmonic materials for analyte sensing[J]. Plasmonics, 2022, 17(5): 2075-2087.

[24]   LIU Y D, JING X L, LI S G, et al. High-sensitivity plasmonic temperature sensor based on gold-coated D-shaped photonic crystal fiber[J]. Applied optics, 2019, 58(18): 5115-5121.

[25]   ZHANG J G, YUAN J H, QU Y W, et al. A surface plasmon resonance-based photonic crystal fiber sensor for simultaneously measuring the refractive index and temperature[J]. Polymers, 2022, 14(18): 3893.

[26]   SARKER S, DHASARATHAN V, STUDNICKA F. Design of a nanoscale gold coated photonic crystal fiber bio-sensor[J]. Frontiers in physics, 2023, 11: 1164255.